ECS Journal of Solid State Science and Technology, 2022 **11** 114002
2162-8777/2022/11(11)/114002/9/$40.00 © 2022 The Electrochemical Society ("ECS"). Published on behalf of ECS by IOP Publishing Limited

Opto-Dielectric Properties of TeO_2-Li_2O-LiCl-Eu_2O_3 Glasses

Zahra Ashur Said Mahraz,[1,2,z] Siti Aishah Jupri,[1] E.S. Sazali,[1] M. R. Sahar,[1] and K. A. Samah[1]

[1]*Advanced Optical Materials Research Group, Department of Physics, Faculty of Science, Universiti Teknologi Malaysia, Skudai 81310, Johor, Malaysia*
[2]*Department of Physics, College of Education-Zulten, University of Sabratha, Libya*

Europium oxide (Eu_2O_3) doped lithium tellurite glasses were prepared via melt quenching method. The effects of Eu_2O_3 doping at varying concentrations on the physical, electrical and optical properties of tellurite glasses were determined. The physical properties utilizing density and molar volume are determined. Electrical and dielectric constant in the 0.01–10 MHz frequency range was monitored as a function of temperature (298–398 K). At room temperature, the conductivity and activation energy increase with an increase in Eu_2O_3 concentration. Small polaron hopping (SPH) is used to explain the conduction mechanism. The density of the localized state is found to decrease with increasing Eu_2O_3 concentration in the range of 21.3×10^{20} to $17^{-3}\times10^{20}$ eV^{-1} cm^{-3}. Dielectric parameters which are dielectric constant and loss tangent are found to increase with the increase in the concentration of Eu_2O_3. To study the spectroscopic properties of fabricated glasses, absorption and emission spectroscopy have been performed. UV–vis-NIR absorption spectra of glass samples divulged two significant peaks. Under the excitation of a 393 nm laser diode, six emission bands were observed in the Eu^{3+} single-doped glasses of which the peak at 613 nm corresponding to the transition $^5D_0 \rightarrow {}^7F_2$ is highly intense for such glasses. Increasing intensity ratio ranging from 1.13 to 2.13 with increased Eu_2O_3 concentration is attributed to the low symmetry environment around Eu^{3+} ions. The findings of the current study can be used in advanced functional optoelectronic applications.
 [DOI: 10.1149/2162-8777/ac9c2f]

Manuscript submitted July 29, 2022; revised manuscript received September 30, 2022. Published November 2, 2022.

Nowadays, the use of oxide glass materials has evolved from simple conventional passive functions to more sophisticated active functions in many optical, electronic, structural, chemical, and biochemical interdisciplinary applications.[1] Among the oxide glasses, tellurium dioxide (TeO_2)-based glasses have been widely studied because of their potential applications as compared to other conventional glasses. This is due to their high indices of refraction, large infrared transparency, high density, low melting point, high dielectric constant and electrical conductivity, and good chemical durability as well as low phonon energy.[1–3] Low phonon energy is critical in reducing nonradiative loss through multiphonon relaxation and promotes radiative transitions.[4] Conversely, TeO_2 is a conditional glass former and it cannot easily transform into a glassy state under conventional quenching conditions. Few modifiers or glass forming agents such as alkali oxides (M_2O) are required to enhance the glass formation ability (GFA) by breaking the Te–O–Te bridging and forming the Te–O–M bonds.[5] Tanaka et al.[6] study the structure of LiCl-Li_2O-TeO_2 glasses and they show that the presence of LiCl and Li_2O creates non-bridging oxygen (NBO). Cl^- and O^{2-} are considered to be fully ionized hence creating the Te–Cl_{eq} bond and Te–O_{eq} bond. Since O^{2-} has a higher negative charge than Cl^-, O^{2-} ion would donate more electrons to Te through the Te–O_{eq} bond than Cl^- ion does through the Te–Cl_{eq} bond. The formation of this bond strengthened the Te–O_{ax} bond therefore the formation of the TeO_3 trigonal pyramid is suppressed. Iwadate et al.[7] state that the TeO_4 trigonal bipyramids are changed into polyhedra containing NBO by the increase of Li_2O and LiCl, and then shifted to TeO_3 trigonal pyramids which are considered to restrict the glass formation. This can be explained by the weakening Te–O_{ax} bond with the increase of LiCl which act as a network modifier. LiCl breaks down the TeO_4 network structure by creating NBO.

The introduction of alkali ions in tellurite glasses is considered to be the predominant factor playing the role of enhancing the conductivity of the glass system and hence can be applied as solid electrolytes in high-density batteries, electrochromic display, fuel cells, and sensors.[8–10] Tellurite-based glasses exhibit relatively high dielectric constants and electrical conductivity as compared to the other glass systems, owing to the unshared pair of electrons of the TeO_4 group that do not take part in the bonding.[11] The dielectric properties of tellurite glasses depend on the size of the modifier ions in the glass structure, their field strengths, and the composition of the glass. The introduction of lithium is anticipated to enhance the conductivity of tellurite glass as Li^+ ions are ionic conductors.[12,13] This is because lithium is light and highly electro-positive. Consequently, lithium-based glasses find potential applications in high energy density solid-state batteries.[14] Hence, the connection between the position of lithium ions in the tellurite glass network and the electrical properties of these glasses is quite interesting.

Incorporation of rare Earth (RE) ions such as La, Ce, Nd, Eu, Er, etc., into glasses, enhance their optical properties such as refractive index, optical band gap, laser amplification, and optical amplification.[12,15–17] Recently, up-conversion (UC) luminescence of Eu^{3+} has been studied due to its favorable green and red emissions. However, it is interesting to study the electrical conductivity in these glasses to understand the conduction mechanisms operated in these systems. The influence of RE ions additives on the electrical conductivity of different glasses has been previously studied,[12,15–18] which indicated that the electrical conductivity depended on the glass composition and atomic size of RE ions.[15] In addition, a decrease in conductivity with the increase in the atomic weight of RE ions has been observed in different rare Earth ions doped tellurite glasses, which was attributed to the low mobility of RE ions due to their heavy masses.[16] Meanwhile, tellurite glasses of composition $80TeO_2$–20ZnO doped with holmium (Ho^{3+}) ions exhibited a decrease in conductivity with the increase in holmium ionic content.[17] This was attributed to the formation of a quasi-molecular complex of RE ions with the glass network. The dc and ac electrical conductivities of barium tellurite borate glass doped with Nd_2O_3 having a composition of $50B_2O_3$-(20-x)BaO-$20TeO_2-10$LiF or Li_2O, where $x = 0.5$, 1, 1.5 and 2 mol% were measured.[12] The dc and ac conductivity values were increased, whereas the activation energy of conductivities was decreased with increasing Nd_2O_3 content in the glasses containing LiF. Whereas, the addition of Nd_2O_3 to glasses containing Li_2O led to a decrease in the conductivity and increased the activation energy.[12]

Amongst RE ions, Eu^{3+} -doped glasses find some applications in a variety of optoelectronic devices such as red-emitting phosphors and optical storage devices.[18] With a suitable selection of glass constituents, one can develop an entire range of electrical conductors, from purely ionic to purely electronic. Glasses with such properties have found applications in the development of integrated

[z]E-mail: mabutm.mabutm@yahoo.com

micro-batteries.[19] For the Eu^{3+} ion, since the red fluorescence is due to the transitions from the $^5D_0$ level, which has much higher energy than the next lower level ($^7F_6$), so the phonon energies of the hosts are not a very essential criterion to obtain the red emission.[20] However glasses with low phonon energy are advantageous to decrease the multiphonon relaxation rate and obtain efficient radiative emissions from the $^5D_0$ level.[21] Besides, the low phonon glasses also provide an opportunity to investigate the unusual emission transitions from the $^5D_1$, $^5D_2$ and $^5D_3$ levels of Eu^{3+} which are rarely observed in hosts of high phonon energy.[22] Despite the technological and scientific relevance of tellurite glasses, the ac conductivity studies in Eu_2O_3 doped lithium-tellurite glasses are far from being clarified. In this fortitude, the objective of the present work is to evaluate the physical, electrical and optical properties of the representative TeO_2-Li_2O-LiCl (TLL) glass doped with different concentrations of Eu^{3+} ions. The electrical and dielectric properties of such glass samples as a function of frequency (100 Hz–1 MHz) and temperature (298K–398 K) were analyzed by employing impedance spectroscopy at 373 K.

Experimental

Analytical grade raw materials to prepare the TeO_2-Li_2O-LiCl-Eu_2O_3 glass samples were obtained in powder form. Pure oxides of TeO_2 (Sigma-Aldrich ⩾99%), Li_2CO_3 (Sigma Aldrich, 99.99% purity), LiCl (Fluka, 99% purity), and Eu_2O_3 (Sigma Aldrich, 99.99% purity) were used as glass constituents. The prepared samples had nominal composition of (75-x) TeO_2−5Li_2O-20LiCl-$x$$Eu_2O_3$ where x = 0.0, 0.5, 1.0, 1.5 and 2.0 mol%. The raw materials with the required proportion are weighed using a very sensitive weighing machine (Electronic Balance Precisa 205 A SCS). The total weight of each batch of glass was 15 grams and calculated in mol%. The selected composition was placed in an alumina crucible and melted by raising the temperature of an electrical furnace (Model: Carbolite Aston Lane, Hope Sheffield S30 2RR, England) to 900 °C for 20 min to achieve homogenous melting. To obtain transparent viscous melt, the batches were stirred frequently. The quenching process started by pouring the melt between two preheated stainless steel moulds in an alternate furnace as fast as possible to avoid solidification due to humidity. Then, the glass samples were kept at 300 °C for about 2 hr for the annealing process to reduce the thermal and mechanical strains. After two hours, the furnace was switched off and the samples were allowed to cool down gradually to room temperature (25 °C). The cooling rate was a vital factor in determining the glass formation. The glass sample is cut in the dimension of 1 cm × 1 cm × 1 cm using a diamond cutter. Finally, samples are polished with a diamond compound with a grade point of 1 μ, 3 μ, and 6 μ until each of the samples has a uniform thickness of ∼0.2 cm.

The glass density (ρ in g.cm^{-3}) is determined using the Archimedes method with distilled water as an immersion liquid. Density is calculated from,

$$\rho = \frac{A_a}{A_a - B_w} \times (\rho_0 - \rho_a) \quad [1]$$

Where A_a and B_w are the weight of the sample in the air and distilled water, respectively with ρ_0 is the density of pure water and ρ_a is that of air. The molar volume (V_m) in terms of the molecular weight (M) yields,

$$V_m = \frac{M}{\rho} \quad [2]$$

The concentration of rare Earth ion, N_{RE} is given by,

$$N_{RE} = \frac{\text{mol\% of RE} \times \rho \times \text{N}_\text{A}}{V_m} \quad [3]$$

where ρ is the density of the glass and N_A is Avogadro's number. The polaron can be treated as an electron with virtual phonon. The cloud of a virtual phonons resembles physically the electron where it pulls nearby positive ions and pushes nearby negative ions away. Assuming the distribution of Eu_2O_3 in lithium tellurite is uniform, the polaron radius R_p can be calculated by the following equation respectively,

$$R_P(\text{Å}) = \left(\frac{1}{2}\right)\left(\frac{\pi}{6N_{RE}}\right)^{\frac{1}{3}} \quad [4]$$

On the other hand, the inter-nuclear distance, $R_i$which denoted the distance between two nuclei in a molecule is calculated as follows,

$$R_i(\text{Å}) = \left(\frac{1}{N_{RE}}\right)^{\frac{1}{3}} \quad [5]$$

The amorphous nature of glasses was examined via a Bruker D8 Advance X-ray diffractometer (XRD) which uses CuKα radiations (k = 1.54 Å) at 40 kV and 100 mA with 2θ ranges from 10° to 80° with step size 0.02° and resolution of 0.01°. Shimadzu ultraviolet-visible near-infrared (UV–vis-IR) spectrophotometer (Model: UV-1301PC) was used to record the absorption spectra of the glass samples with a resolution of 1 nm. The absorption spectrum was measured in the spectral range of 200–2000 nm by using a Tungsten Halogen lamp (HL) as a radiation source. Both sides of the glass samples were polished to avoid any unfavorable surface scattering during optical measurements. Perkin-Elmer photoluminescence (PL) spectra (Model: LS 55) (fitted with a pulsed Xenon lamp that operates as a source of excitation) were used to measure the emission spectrum of the glass samples in visible (∼400 to 700 nm) and the near-infrared region (up to 800 nm). Gold electrodes are deposited on both sides of the polished glass sample using the thermal evaporation technique. The conductivity measurement is done using Solartron SI 1260 Impedance/Gain-Phase Analyzer. The measurement is taken in the frequency range of 100 Hz to 1 MHz and in the temperature range of 298 K to 398 K and the voltage is kept constant at 1 V. To avoid initial polarization, the measurements are started 5 min after the voltage across samples is constant. Measurements are repeated several times to ensure the reproducibility of the data.

Table I. Density, ρ (g.cm^{-3}), ion concentration, N_{RE} (×10^{20} ions.cm^{-3}), molar volume, V_m (cm^3.mol^{-1}), polaron radius, R_p(Å) and inter-nuclear distance, R_i(Å) of Eu^{3+}-doped lithium tellurite glass.

Glass Sample	ρ	V_m	N_{RE}	R_p	R_i
TLLE 0.0	4.88 ± 0.01	26.4 ± 0.2	—	—	—
TLLE 0.5	4.73 ± 0.02	27.5 ± 0.1	1.10	8.42	20.89
TLLE 1.0	4.74 ± 0.01	27.6 ± 0.1	2.18	6.70	16.61
TLLE 1.5	4.76 ± 0.03	27.7 ± 0.2	3.26	5.86	14.54
TLLE 2.0	4.77 ± 0.03	27.8 ± 0.2	4.33	5.33	13.22

Results and Discussion

Physical properties.—Table I summarizes the calculated physical properties of all glass samples. Compositional behavior of density and molar volume is shown in Fig. 1. The decrease in glass density from 4.88 to 4.73 g.cm^{-3} due to the introduction of Eu_2O_3, which is ascribed to the alteration in the network structure via the generation of more NBOs. However, the density of the glass increases from 4.73 to 4.77 g.cm^{-3} with further addition of Eu_2O_3, which is due to higher charge and coordination number of Eu^{3+} which tend to develop highly packed glass structure.[23] The variation of molar volume with a concentration of Eu_2O_3 is presented in Fig.1. It is quite clear from Fig. 1 that there is an increase in the molar volume from 26.4 to 27.8 cm^3.mol^{-1} as the concentration of Eu_2O_3 is increased into the system. The molar volume is inversely

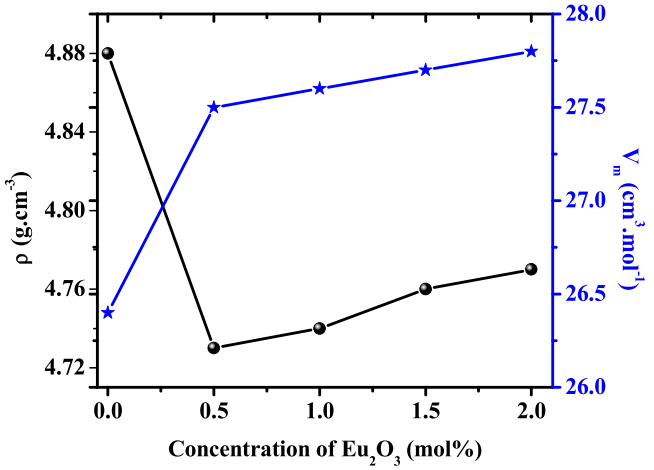

Figure 1. Compositional variation of density and molar volume of TLLE*x* glasses.

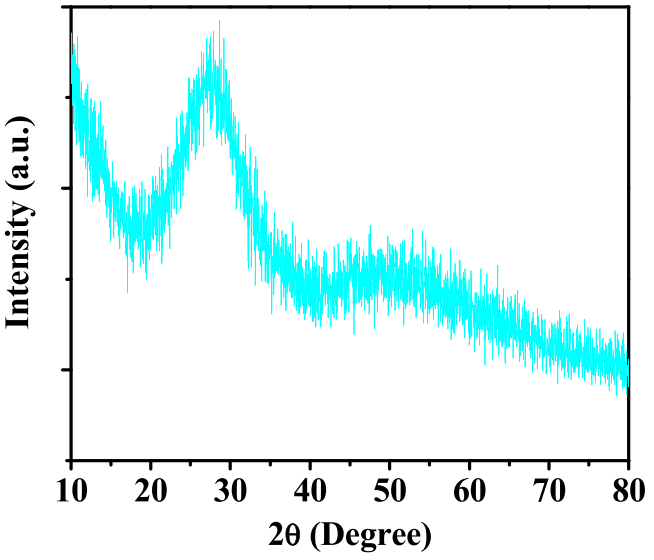

Figure 2. Eu^{3+} ions concentration (mol%) dependent XRD patterns of TLLE 2.0 glass sample.

proportional to density and they are expected to show opposite behavior to each other. However, in this glass system, the molar volume shows the same behavior as the glass density where they both increase with the increase of Eu_2O_3 concentration. Sidek et al.[24] stated that the molar volume is affected by the bond length or inter-atomic spacing between atoms. In this glass system, TeO_2 is replaced by Eu_2O_3 where the bond length of Te–O and Eu–O are 1.99 Å and 2.04 Å, respectively. On the other hand, their respective ionic radius is 0.52 Å and 0.947 Å. The replacement of Eu_2O_3 with the longer bond length and ionic radius is believed to contribute to the increment of molar volume. This also indicates that the addition of Eu_2O_3 may break the structure of the glass by the formation of NBOs. Consequently, the spatial distances in the system increase and loosen the structure.[25] Rada et al. suggest that the increase in molar volume is due to the excess oxygen from Eu_2O_3 that is not filling the interstices of the glass network but forming the Eu–O–Eu bond.[26]

The ion concentration, polaron radius and inter-nuclear distances are also calculated, and summarized in Table I. A direct relation between the increases in ion concentration with increasing Eu^{3+} ions is evident. An inverse relation is observed between the ion concentration and inter-nuclear distance. Thus a perfect connection for the

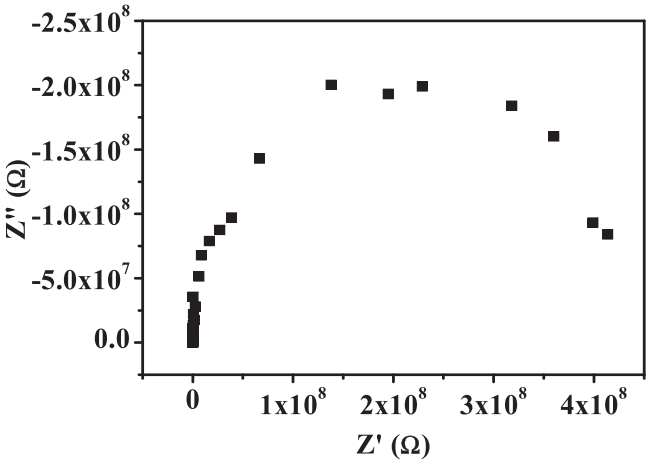

Figure 3. Complex impedance plots of TLLE 0.0 glass at 373 K.

current samples could be expected. In contrast, the polaron radius and inter-nuclear distance for Eu-Eu ions show an expected decrease in increasing Eu_2O_3 content. This is most likely due to the glass system becoming packed by rare Earth existence hence average rare Earth-oxygen distance decrease.[27] However, the value of polaron radius is smaller (8.420 Å–5.326 Å) than the inter-nuclear distance (20.893 Å–13.215 Å) which suggests the formation of small polaron.

XRD pattern.—Figure 2 displays the typical XRD pattern of TLLE 2.0 glass. The complete absence of any sharp peak in the XRD pattern and the appearance of a broad hump in the angular range of 15°–35° verified the true amorphous nature of the proposed glass. The occurrence of the halo pattern indicated the absence of long-range atomic arrangement or three-dimensional network periodicity in the prepared material.

Ionic conductivity.— *Temperature-dependent conductivity.*—A deeper insight into the electrical properties of the glasses can be obtained from the complex impedance plane plot analysis. The impedance ($Z''(\omega)$ and $Z'(\omega)$) in the frequency range of 100 Hz–1 MHz of the studied glasses were recorded and found to exhibit non-ideal semicircle (Cole-Cole plots) which could be originated from the dielectric dispersion in the glasses. The typical complex impedance cole-cole plots (Nyquist plots) obtained at a representative temperature, 373 K, for the case of TLLE 0.0 glass is depicted in Fig. 3. The cole-cole diagram of all the investigated glasses exhibited similar behavior with a single semicircle which specified a single relaxation process. Table II enlists the estimated values of cole-cole parameters of studied glasses and their codes. The presence of an inclined spike (and arc) on the lower frequency side of the semicircle has resulted from the ionic adsorption and accumulation at the interface with the blocking electrode, as well as charge transfer.[28] Therefore, the conductivity of the glass system was assumed as mainly ionic. This behavior of cole-cole plots was characteristic of the conducting nature of the glass samples. The intercept of the semicircle with the real axis on the low-frequency side was normally referred to as the bulk resistance (R_b) of the glass samples. The bulk resistance of the glass can be obtained through circle fit by using ZView Version 2.5b. The intercept of the semicircle was shifted towards the higher Z' value with the increase of Eu^{3+} ions content, indicating the increase in the bulk resistance and thereby decreasing conductivity. From Fig. 3, the magnitude of conductivity can be calculated as follows:

$$\sigma = \frac{d}{R_b A} \qquad [6]$$

where d is the thickness of the sample and A is the area of conductance of the sample. The variation of conductivity of these

Table II. Bulk resistance, R_b ($\times 10^8$ Ω) and conductivity, σ ($\times 10^{-7}$ Scm^{-1}) of the proposed glass samples at constant frequency.

		TLLE 0.0			TLLE 0.5			TLLE 1.0			TLLE 1.5			TLLE 2.0		
K	10^3/T	R_b	σ	Log σ	R_b	σ	Log σ	R_b	σ	Log σ	R_b	σ	Log σ	R_b	σ	Log σ
298	3.36	5.01	1.33	−6.88	6.08	1.02	−6.99	5.59	1.25	−6.90	6.05	0.98	−7.01	6.27	1.05	−6.98
323	3.10	4.69	1.42	−6.85	6.06	1.03	−6.99	6.20	1.66	−6.78	6.12	0.97	−7.01	5.68	1.16	−6.94
348	2.87	4.26	1.56	−6.81	5.46	1.14	−6.94	5.14	2.01	−6.70	5.39	1.10	−6.96	4.50	1.46	−6.83
373	2.68	4.35	1.53	−6.82	4.63	1.34	−6.87	4.30	2.40	−6.62	5.38	1.10	−6.96	4.46	1.47	−6.83
398	2.51	4.11	1.62	−6.79	4.17	1.49	−6.83	4.00	1.74	−6.76	4.49	1.32	−6.88	4.13	1.59	−6.80

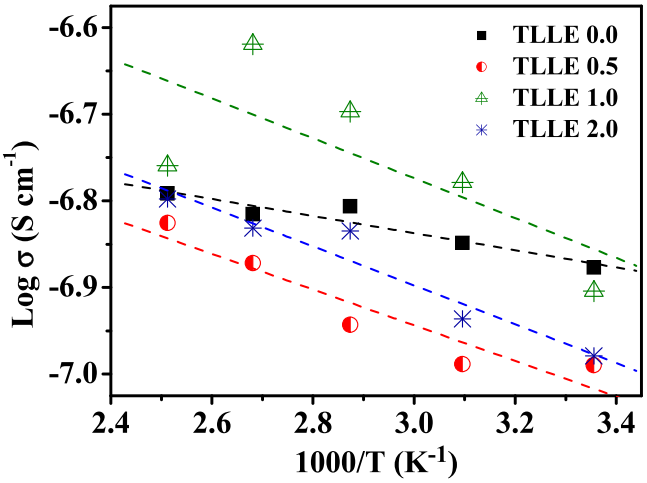

Figure 4. Arrhenius relation of Log(σ) vs 1000/T for all samples.

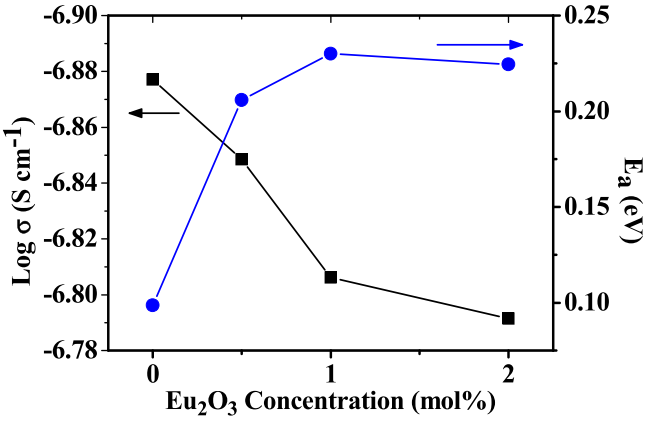

Figure 5. Variation of Log(σ) and activation energy for TLLE*x* glasses.

glasses can be well represented by the Arrhenius equation.

$$\sigma = \sigma_0 \exp\left(-\frac{E_a}{k_B T}\right) \quad [7]$$

where E_a is the activation energy, σ_o is the pre-exponential factor, K_B is Boltzmann's constant; 8.617×10^{-5} eV K^{-1}, and T is temperature. The variation of the corresponding conductivities for the TLLE*x* series of glasses is shown in Fig. 4 in a semi-log plot as a function of inverse temperature.

The conductivity was found to increase with the increase in temperature (see Table II), which reveals the semiconducting nature of the present glass samples.[29] The charge carrier may be thermally stimulated at higher temperatures. The increasing temperature decreases the electrostatic binding energy which eases the mobility

Table III. Values of E_a, ε', tan δ and N (E_F) ($\times 10^{20}$ eV^{-1} cm^{-3}) for different compositions of glasses at 398 K and in the relaxation frequency.

Studied glass	E_a	ε'	tan δ	N (E_F)
TLLE 0.0	0.10	17.70	0.097	21.3
TLLE 0.5	0.21	13.48	0.087	19.7
TLLE 1.0	0.23	11.52	0.078	23.0
TLLE 1.5	0.23	10.63	0.073	19.8
TLLE 2.0	0.10	9.81	0.055	17.3

of Li^+ ions, henceforth the conductivity increases.[30] The electrical conductivity, at all studied frequencies, decreased with an increase in the rare Earth ion concentration. On the other hand, the activation energy is the amount of electrostatic term which combines the mean barrier height created by the Coulomb forces and the energy of migration.[31] The activation energy (E_a) is calculated from the slope fitting lines using Eq. 7 and is shown in Fig. 5. In Table III, the values of the activation energy have been presented at different concentrations of Eu_2O_3. From Fig. 5, it can be seen that the conductivity decrease while the activation energy increase with an increase in Eu_2O_3 concentration. The dependence of conductivity on activation energy suggests that the decrease in conductivity is directly related to the decrease in the movement of lithium ions.[32] The decrement in the conductivity can be related to the addition of Eu_2O_3 which leads to the increase in density of the glass network. In addition, the heavy atomic mass of the RE partially prevented the lithium-ion movement thus leading to the decrement of conductivity.[29,32] The activation energy increased from 0.10 eV to 0.23 eV as the concentration of Eu_2O_3 increased. It is suggested that the more Eu_2O_3 is added to the glass network, the glass becomes packed. Hence, the vacant sites for Li^+ mobility decrease. This leads to the reduction of polaronic hopping distance. Therefore, more energy is required for charge carrier transportation.[16,22]

Frequency dependence conductivity.—To describe the influence of frequency on the conductivity of a material, Jonscher suggested a suitable formula acknowledged as power-law relation[33] which can be expressed as:

$$\sigma(\omega) = A\omega^s \quad [8]$$

The exponent s represents the degree of interaction between mobile ions with the lattices around them, while the prefactor exponent A determines the strength of polarizability and ω is the angular frequency. Therefore, s is defined as:

$$s = \frac{\partial(\log \sigma)}{\partial(\log \omega)} \quad [9]$$

The straight line is obtained by the least square fitting of experimental data. Various models have been proposed to ascertain the conduction mechanism based on parameter s. Among these models, the quantum mechanical tunneling model (QMT), correlated

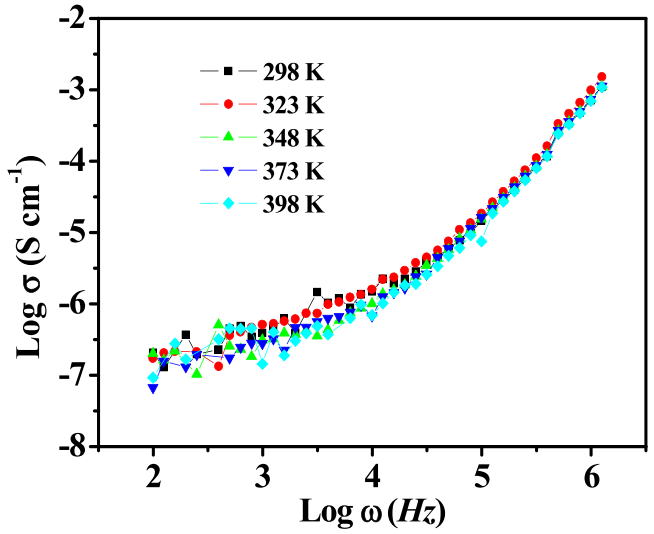

Figure 6. Frequency dependence of the conductivity, σ_{ac}(T), at temperatures shown for the TLLE glass doped 1.5 mol% Eu_2O_3.

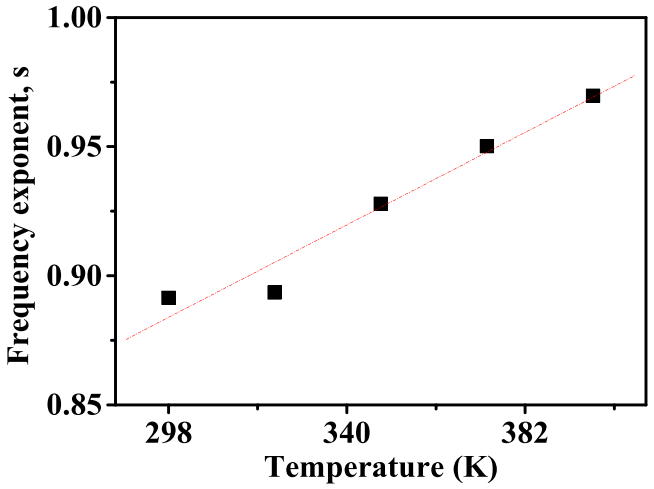

Figure 7. Variation of the exponent parameter, *s* with temperature for TLLE 2.0 glass.

barrier hopping model (CBH), small polaron hopping (SPH) and the overlapping large-polaron (OLP) is the most applicable models.

The frequency dependence of total conductivity for 1.5 mol% Eu_2O_3-doped glass at different temperatures is shown in Fig. 6. Similar nature of variation of log(σ_{ac}) with log(ω) has been observed in the remaining samples. A flat dc plateau can be observed (Fig. 6) at low frequencies. From Fig. 6 it can be noticed that the ac conductivity (σ_{ac}) increases as the frequency increases. The frequency dependence of ac conductivity indicates that conduction is attributed to the increase of the thermally activated small polarons hopping (SPH).[29,34] The polaron comprises the electron plus its surrounding lattice deformation. (polarons can also be formed from holes in the valence band). If the deformation extends over many lattice sites, the polaron is "large" and the lattice can be treated as a continuum. Charge carriers induce strongly localized lattice distortions from small polarons.[35] At the high frequency, end the curves overlap indicating the possibility of the presence of space charges. This assumption is reasonable since the space charge effect vanishes at higher temperatures and frequencies. Also, it is observed that the power law fit is good throughout the frequency range, hence single exponent fit seems to be adequate.

To determine the predominant conduction mechanism of the ac conductivity for the sample, one can suggest the appropriate model

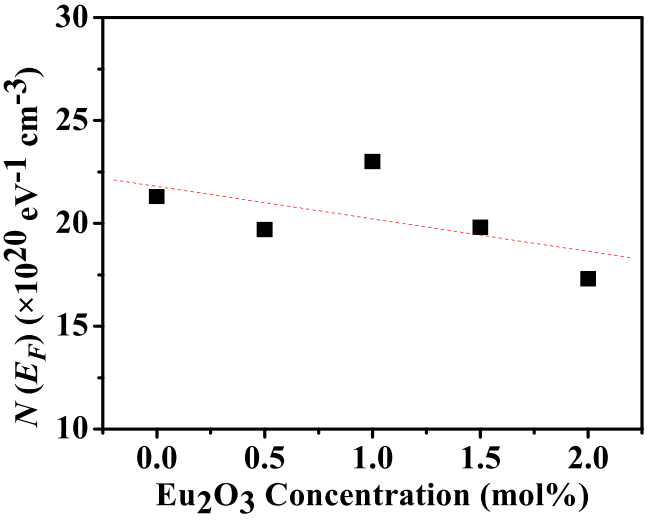

Figure 8. The calculated density of localized state, $N(E_F)$ as function of Eu_2O_3 concentration at 298 K.

for the conduction mechanism in light of the different theoretical models correlating the conduction mechanism of ac conductivity with *s*(T) behavior. If *s* is temperature independent, QMT is expected. The CBH is usually associated with a decrease in *s* with temperature. SPH conduction is predominant if *s* increases with temperature. In the OLP conduction mechanism, *s* decreases with the temperature reaching a minimum value and then increases again. For the presently studied glass samples, the frequency dependence of *s* has increasing trends with temperature, suggesting the SPH model (Fig. 7). The ac conductivity and frequency exponent expressions of the SPH model are given by the following equations:

$$s = 1 - \frac{4}{\ln\left(\frac{1}{\omega\tau_0}\right) - \frac{W_H}{K_B T}} \quad [10]$$

where τ_0 is the characteristic relaxation time which is of the order of $\tau_0 = 10^{-13}$ s, W_H is energy for polaron transfer, and T is the temperature. Generally, for ionic conductivity, the power law exponents (*s*) may lie between 1 and 0.5, representing ideal long-range pathways and diffusion-limited hopping.[36] In our work, *s* it is less than unity, the result suggests the polaron conduction.

According to this model, the ac conductivity is given by the following equation:

$$\sigma_{ac} = \frac{(\pi e)^2 k_B T \alpha^{-1} \omega [N(E_F)]^2 R_\omega^4}{12} \quad [11]$$

Where

$$R_\omega = \frac{1}{2\alpha}\left[\ln\left(\frac{1}{\omega\tau_0}\right) - \frac{W_m}{k_B T}\right] \quad [12]$$

where α^{-1} is the spatial extension of the polaron, $N(E_F)$ is the density of states near the Fermi level, R_ω is the tunneling distance and $W_m$is the maximum height of the barrier over which carriers must hop.

Using Eq. 11, the density of defect energy state, $N(E_F)$ at 298 K is obtained and listed in Table III. From Table III, a plot of the density of defect energy state against Eu_2O_3 concentration can be made and is shown in Fig. 8. It can be seen that the value of $N(E_F)$ obtained is found to be around $\sim 10^{20}$ eV^{-1} cm^{-3} which suggest that the localized states are near Fermi level.[37–39] The value of $N(E_F)$ is found to be decreased from 21.3×10^{20} eV^{-1} cm^{-3} to 17.3×10^{20} eV^{-1} cm^{-3} as the concentration of Eu_2O_3 increased. This can

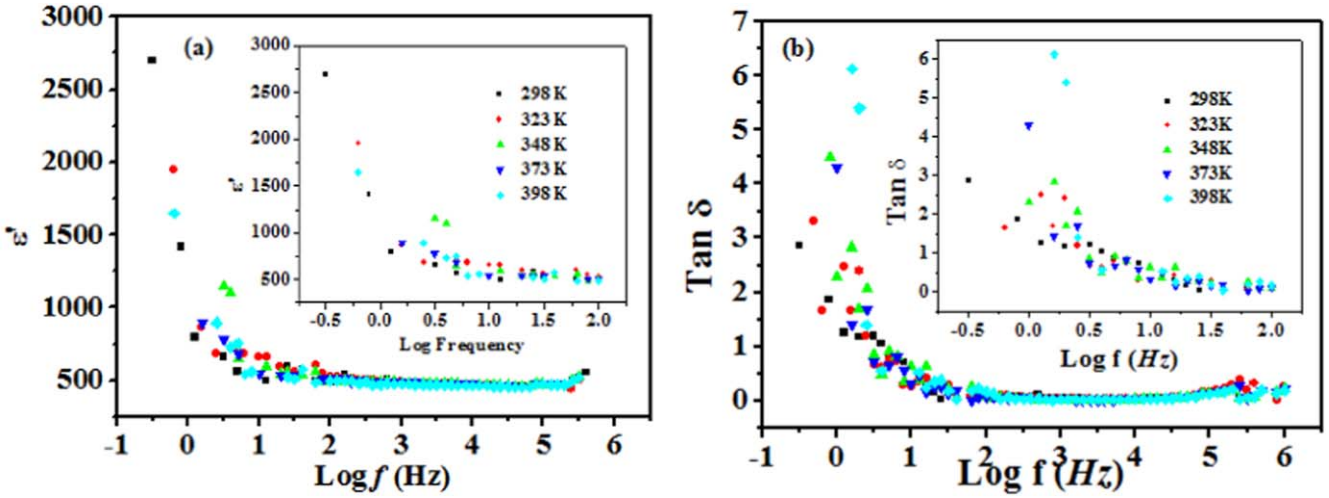

Figure 9. The frequency dependence curves at room temperature of dielectric constant $\varepsilon'(\omega)$ (a) and loss factor (b) for TLLE1.5 glass sample. Inset shows the variation of $\varepsilon'(\omega)$ and tan(δ) at different temperatures case of 1.5 mol% Eu_2O_3.

be explained by the decreasing disorder in the glass network.[40] The introduction of Eu_2O_3 into the glass leads to the creation of quasi-molecular complexes which is the condition where the rare Earth coordinated to the non-bridging oxygen which is attached to the glass network at one end. The formation of quasi-molecular complexes is believed to have a reasonably constant coordination polyhedron.[17] The lowering value of $N(E_F)$ also indicates the decreasing presence of charge carriers in the glass network.[41]

Dielectric investigation.—Dielectric relaxation studies are important to understand the nature and the origin of dielectric losses, which may be useful in determining the structure and defects in solids. The dielectric relaxation is described by a cole-cole model. Dielectric properties of glasses are complex functions of frequency, shape, dimension, and spatial ordering of the constituent atoms. The real (ε') and imaginary (ε'') parts of the dielectric constant were calculated via:

$$\varepsilon' = \frac{Cd}{\varepsilon_0 A} \quad [13]$$

and

$$\tan\delta = \frac{\varepsilon''}{\varepsilon'} \quad [14]$$

where C is the capacitance of the sample, ε_0 is the permittivity of free space (8.8542×10^{-12} F m^{-1}), A^{-1} is the cross-sectional area of the electrode, and tanδ is the dissipation factor or loss tangent. The frequency dependence of the dielectric constant (ε') and loss factor (tan δ) are studied for the TLLE 1.5 glass sample and shown in Figs. 9a and 9b. The temperature dependence of ε' and tan δ (case of TLLE 1.5 glass sample) as a function of logarithmic frequency at several temperatures is depicted in Inset of Figs. 9a and 9b. It is observed that the dielectric constant measured at lower frequencies is greater than the higher frequency at all temperatures. The larger values of dielectric constant at low frequencies are attributed to the role of more charge carriers at the interfaces, which can contribute to increasing net dipoles on the interface. These dipoles alter the net polarization of the ionic medium, which contributes to the dielectric constant. Whereas at higher frequencies, the periodic reversal of the applied field takes place so quickly in such a way that there is less time for polarization to form completely and no charge buildup at the interface resulting in a constant ε' value. Atomic and electronic polarization usually occurs at a higher frequency. In accumulation, as shown in the insert of Fig. 9, the value of the dielectric constant shows a considerable increase with temperature and the increment is more pronounced at frequencies lower than 100 Hz. The increasing dielectric constant with temperature can be explained by the weakening of bond energy. Hence, the intermolecular forces decrease which increases orientational vibration.[14,42] The charge carrier acquired thermal energy hence they can move freely within the glass network.[43]

The dielectric constant, ε', and Dissipation factor (tan δ) are tabulated in Table III. The dielectric constant is observed to decrease from 17.70 to 9.81 with Eu_2O_3 concentration. Such behavior is similar to that exhibited by ac conductivity. The large molecular mass of Eu_2O_3 acts as a hindrance to the mobility of the charge carrier, hence there is a decrease in electronic polarization contribution to the total polarizability.[14,29] Electronic polarization is part of the total polarization where it is a polarization that occurs due to the displacement of valence electrons relative to the positive nucleus.[44]

The dissipation factor (tan δ) measures the inefficiency of the insulator. When an insulator is applied to an electric field, heat is emitted due to the high resistance of the insulator. From Fig. 9b, the increasing value of the dissipation factor with increasing temperature is more pronounced at a frequency below 100 Hz. However, it starts to decrease at a higher frequency and remains almost constant. The dissipation factor dependence of frequency is associated with losses by conduction or mobility of charge carriers inside the glass network in addition to the electron polarization loss.[45] The high value of dissipation factor at low frequency suggests that charge carriers can move around hence promoting dielectric loss. As the frequency increase, the mobility of charge carriers decreases hence ion vibration is the only source of dielectric loss.[29]

From Table III, it is observed that the dissipation factor decrease from 0.097 to 0.055 with increasing Eu_2O_3. This is due to the heavy mass of Eu_2O_3 (351.93 g mol^{-1}) that acts as a hindrance to the movement of the charge carrier. The suppressed movement of the charge carrier leads to the decreasing conductivity and dielectric loss. With Eu^{3+} acting as a hindrance to the movement of Li^+ ions, there is a decrement in electronic contribution to the total polarizability.[14,29]

Optical properties.— *Absorption spectra.*—The room temperature UV–vis-NIR absorption spectra recorded in the range of 350–700 nm of selected glass samples are presented in Fig. 10. The absorption bands located at 464 and 533 nm were ascribed to the electronic transitions from $^7F_0 \rightarrow {}^5D_2$ and $^7F_1 \rightarrow {}^5D_1$ of Eu^{3+} ions, respectively. Overall, the spectral profile of every sample was altered accompanied by a slight peak shift for each band. These alterations in the absorption peak positions were attributed to the Stark splitting of the degenerate *4 f* levels in the presence of the host material's crystalline field. This observation indicated the homogeneous incorporation of Eu^{3+} ions (without agglomeration) into the tellurite

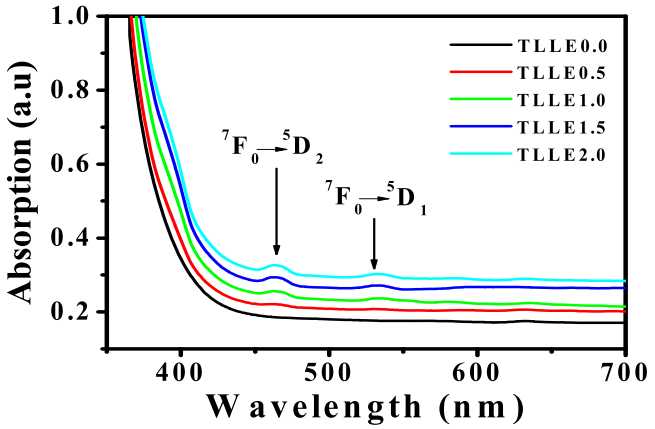

Figure 10. Absorption spectra of glass samples in the UV–vis region.

glass network. Moreover, the slight peak shift was ascribed to the variation of ligand field strength at the REIs site. Generally, the *4f* inner shell behaviour of REIs is not affected by the surrounding Eu^{3+} ions that produce effective shielding on *4f* electrons by the filled *5S* and *5P* shells. This creates more intense lower energy bands compared to the higher ones.[46]

The Davis and Mott theory[47] was used to evaluate the direct and indirect optical band gap energy of the amorphous materials. In both transitions, the electromagnetic waves interact with the electrons in the valence band across the fundamental gap and rise to the conduction band.[48,49] According to Davis and Mott, the absorption coefficient $\alpha(\upsilon)$ can be expressed as a function of photon energy ($h\upsilon$) for the direct and indirect allowed transition:

$$\alpha(\upsilon) = B\frac{(h\upsilon - E_g)^r}{h\upsilon} \quad [15]$$

where r is the index number. In Figs. 11a and 11b, the Tauc's plots of the TLLE*x* glass sample are drawn between $(\alpha h\upsilon)^{1/n}$ and photon energy ($h\upsilon$), by substituting the value $r = 1/2$ in Eq. 15 for direct allowed transitions and $r = 2$ for indirect allowed transitions. Here, B is constant, E_g is the optical band gap and $\alpha(\upsilon)$ is the absorption coefficient represented by:

$$\alpha(\upsilon) = \frac{2.303A}{t} \quad [16]$$

where t is the thickness of the sample and A corresponds to absorbance. The optical band gap values were obtained from the linear part of the curves extrapolating at $(\alpha h\upsilon)^2 = 0$ and $(\alpha h\upsilon)^{1/2} = 0$ for direct and indirect transitions, respectively. The absorption coefficient $\alpha(\upsilon)$ near the absorption band edge exhibits an exponential behavior on the photon energy ($h\upsilon$) and obeys the empirical relation given by Urbach.[50]

Table IV. Direct, E_{dir} (eV), and indirect, E_{ind} (eV) band gaps and Urbach energy, $_{\Delta E}$ (eV) of the proposed TLLE*x* glasses.

Glass Sample	E_{ind}	E_{dir}	ΔE
TLLE 0.0	3.07 ± 0.01	3.29 ± 0.01	0.226 ± 0.001
TLLE 0.5	3.01 ± 0.01	3.26 ± 0.01	0.230 ± 0.002
TLLE 1.0	2.99 ± 0.01	3.20 ± 0.01	0.280 ± 0.002
TLLE 1.5	2.98 ± 0.01	3.19 ± 0.01	0.290 ± 0.002
TLLE 2.0	2.97 ± 0.01	3.17 ± 0.01	0.308 ± 0.001

$$\alpha(\upsilon) = \alpha_0 \exp(h\upsilon/\Delta E) \quad [17]$$

where α_0 is a constant and δE is the Urbach energy which is calculated by the inverse slope of the ln α against $h\upsilon$ in the lower photon energy level. This exponential behavior is due to the band tails associated with the valence and conduction bands which extends into the band gap.

The values of band gaps and Urbach energy of the prepared samples are listed in Table IV. The results in Table IV depict that the direct and indirect optical band gaps decrease from 3.29 and 3.07 eV to 3.17 and 2.97 eV, respectively, as the concentration of Eu^{3+} ions is increased up to 2 mol%. The decreasing value of optical band gap energy by increasing the Eu_2O_3 content can be understood in terms of the structural change that are taking place. It is generally accepted that the location of the absorption edge depends on the oxygen bond strength in the glass-forming network.[51] The introduction of RE changes the oxygen bonding in the glass forming network and any change of oxygen bonding in the glass network such as the formation of non-bridging oxygen (NBO) changed the absorption characteristics. Conversely, when one molecule of Eu_2O_3 was introduced into the tellurite matrix, the coordination number of Te atoms was changed. The optical band gap was influenced not only by the chemical composition but also by the structural arrangement of the host matrix. It has been shown from ab initio molecular orbital calculations that the difference between Homo- and Lumo-state is low for TeO_4 units whereas it is high for TeO_3[52] and even for TeO_{3+1} units.[53] It signified that a broader optical band gap can be observed for TeO_2 - based glasses if the density of TeO_3 and/or TeO_{3+1} unit assisted significantly in the network formation. However, these changes were not sufficient to account for the observed decrease in the optical band gap. With the substitution of Li into TeO_2, bridging Te–O–Te bonds are broken and non-bridging Te–O–Li^{2+} bonds were formed. The NBO bonds have a much greater ionic character and much lower bond energies. Consequently, the NBO bonds have higher polarizability and cation refractions.[52,53]

The existence of δE or band tail in the forbidden energy band gap in glass and amorphous materials represented the disorder in the material.[25] The value of the Urbach energy of the TLLE*x* glass

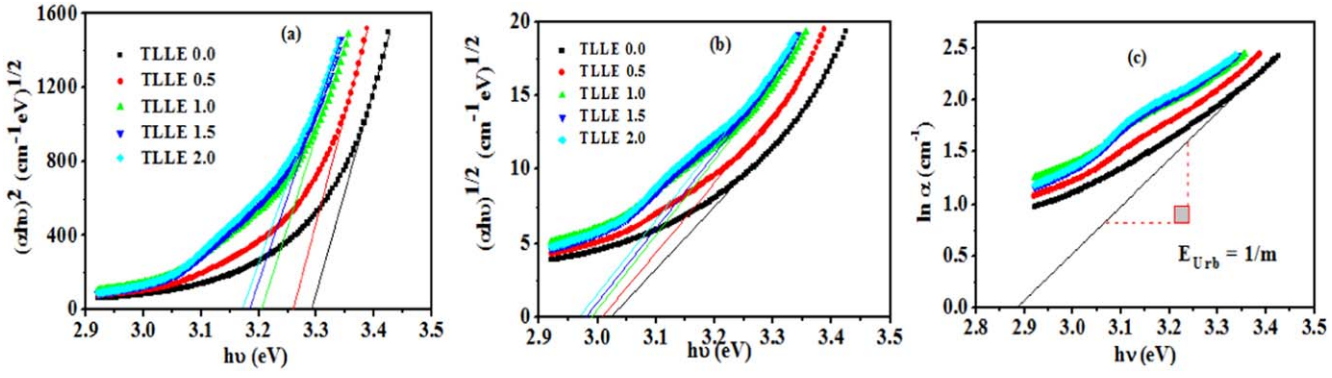

Figure 11. The values of band gap energy for (a) indirect, (b) direct allowed transitions and the (c) Urbach energy for the prepared glass sample.

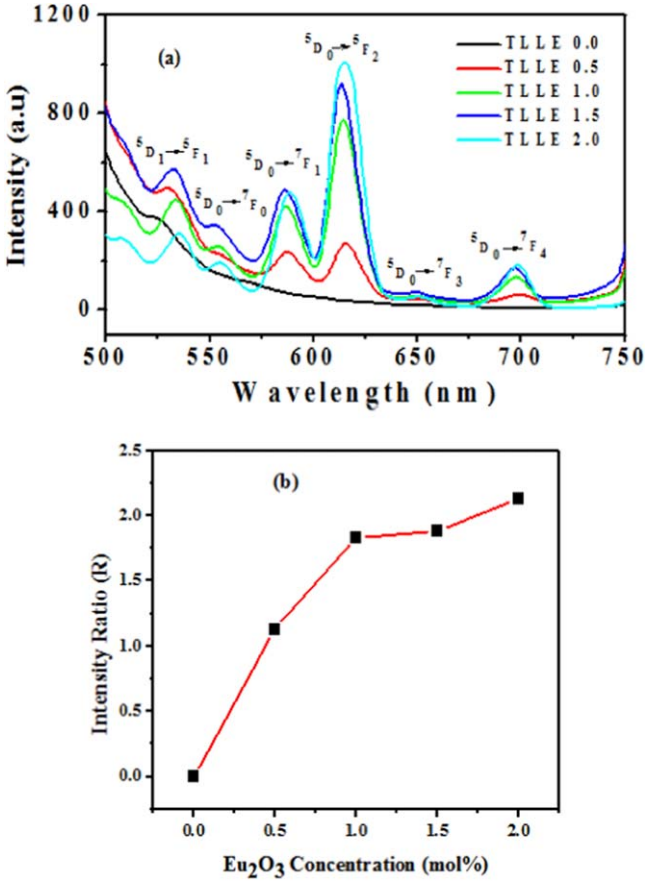

Figure 12. (a) Photoluminescence spectra of the prepared glasses and (b) intensity ratio against Eu_2O_3 concentration.

sample is shown in Fig. 11c. In Table IV, the δE values of the synthesised glasses were found to be increased from 0.226 to 0.308 eV with the addition of Eu^{3+} content. It was evident that by increasing the concentration of Eu^{3+} ions in the present glass system, Urbach energy values were increased due to the increased disorder it the glass.

Photoluminescence spectra.—The room temperature PL spectrum for samples without and with Eu_2O_3 is shown in Fig. 12a, in the range of 500–750 nm upon 393 nm excitation. The relative luminescence intensity peak of such glasses is shown in Fig. 12b. Six evidenced emission bands centered at 532 (green), 552 (deep-green), 586 (orange), 613 (red), 649 (deep-red) and 697 nm (deep-red) nm were assigned to the transitions of $^5D_1 \rightarrow {}^7F_1$, $^5D_0 \rightarrow {}^7F_0$, $^5D_0 \rightarrow {}^7F_1$, $^5D_0 \rightarrow {}^7F_2$, $^5D_0 \rightarrow {}^7F_3$ and $^5D_0 \rightarrow {}^7F_4$ of Eu^{3+} ion, respectively. An increase in the efficient emission was observed (Fig. 12b) with the increase of Eu_2O_3 content up to 2.0 mol%. As the concentration of RE species was increased up to a certain value the optical gain showed an increasing trend.

A sharp peak with the highest intensity is observed at transition $^5D_0 \rightarrow {}^7F_2$ (613 nm) which is in the red region. The $^5D_0 \rightarrow {}^7F_J$ ($J =$ 2 and 4) transitions are electric dipole (ED) transitions while another transition $^5D_0 \rightarrow {}^7F_1$ (586 nm) could be found as magnetic dipole transition.[54,55] Electric dipole transition has a greater probability than the magnetic dipole transition when Eu^{3+} ions are located in a low symmetry environment.[56] On the other hand, the presence of transition $^5D_0 \rightarrow {}^7F_0$ (552 nm) indicated the low symmetry environment of lithium tellurite glass upon the presence of Eu^{3+} ion.[57] This can be confirmed by the intensity ratio which has the formula as follows:

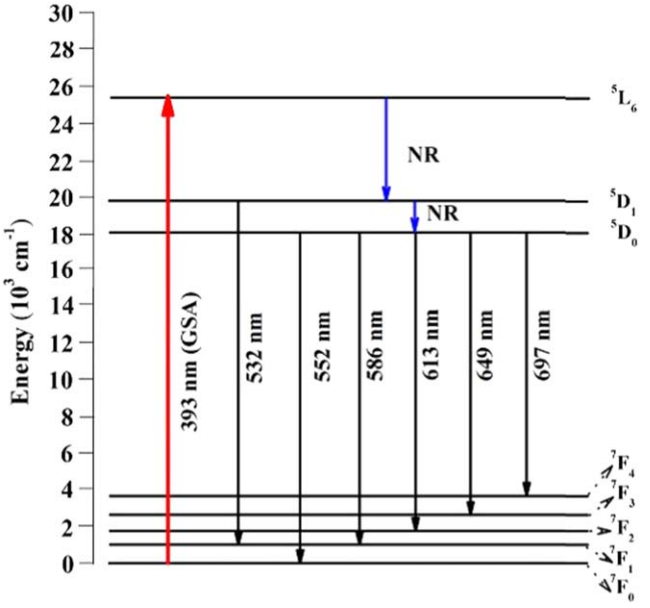

Figure 13. Energy level diagram of the prepared glass system (GSA and NR signify ground state absorption and nonradiative processes respectively).

$$R = \frac{I(^5D_0 \rightarrow {}^7F_2)}{I(^5D_0 \rightarrow {}^7F_1)} \quad [18]$$

The intensity ratio, R indicates the symmetry around Eu^{3+} ions whereas a higher value of R shows that the symmetry around Eu^{3+} is lower.[58] The calculated R for all sample are shown in Fig. 12. A higher value of R shows a better quality of host matrix for laser application.[59] The R values of the presented lithium tellurite glasses are found to be 1.13, 1.83, 1.88, and 2.13 for TLLE 0.5, TLLE 1.0, TLLE 1.5, and TLLE 2.0 glasses respectively. With considerately high R values of glass samples, TLLE 2.0 is suggested for potential laser applications. The region around Eu^{3+} becomes more asymmetry with an increment of Eu_2O_3 addition.[58] The Eu^{3+} ions break the Te–O–Te linkage and create non-bridging oxygen around the structure. Therefore, the structure around the dopant becomes random and irregular. The intensity ratio of the prepared glasses is comparatively on the higher side than the other reported Eu^{3+} doped oxide glass.

The possible energy level of Eu^{3+} in lithium tellurite glass is shown in Fig. 13. From Fig. 13, upon the excitation at 393 nm, the Eu^{3+} ions are excited from $^7F_0$ to $^5L_6$ level by ground state absorption. Nonradiative decay through multiphonon relaxation takes place which results in the population of $^5D_0$ and $^5D_1$ levels. As the result, transitions $^5D_1 \rightarrow {}^7F_1$ and $^5D_0 \rightarrow {}^7F_J$ ($J = 0, 1, 2, 3, 4$) can be observed throughout the spectra. This is in agreement with other researchers.[36,58,60]

Conclusions

We examined the physical, optical, and dielectric properties of Eu_2O_3 doped lithium tellurite glasses synthesized via the melt quenching method. Glasses were characterized using various analytical tools. The influence of Eu^{3+} dopant concentration on conductivity, dielectric constant and loss tangent are determined using the Impedance Analyzer. The temperature dependence conductivity is found to follow the Arrhenius equation. The conductivity decrease while activation energy, E_a increase with Eu_2O_3 concentration. The frequency-dependent conductivity is found to follow the power law. The density of states is calculated using the SPH model and found to decrease with

Eu_2O_3 concentration. The dielectric constant and loss tangent decrease with both frequency and Eu_2O_3 concentration. The optical band gap energy value for the direct and indirect allowed transitions occurred in the range of 3.29 and 3.07 eV to 3.17 and 2.97 eV, respectively. The PL spectra revealed six prominent peaks with a gradual increase in the peak intensity as a function of Eu^{3+} ions doping. The Eu^{3+} ions possess prominent laser luminescence in the red region at transition $^5D_0 \rightarrow {}^7F_2$ (613 nm). Subsequently, these samples have high potential for the application in optoelectronic devices.

Acknowledgments

The authors would like to express their gratitude to the Government of Malaysia through grant vote 03E78 for the financial support of this project. Thanks are also due to UTM through RMC for awarding the Postdoctoral fellowship to the first author.

ORCID

Zahra Ashur Said Mahraz https://orcid.org/0000-0002-9424-4430

References

1. M. Rajesh, G. R. Reddy, N. J. Sushma, G. Devarajulu, and B. D. P. Raju, *Optic. Mater.*, **107**, 110038 (2020).
2. G. Lakshminarayana, K. M. Kaky, S. O. Baki, A. Lira, P. Nayar, I. V. Kityk, and M. A. Mahdi, *J. Alloys Compd.*, **690**, 799 (2017).
3. M. R. Dousti, P. Ghassemi, M. R. Sahar, and Z. A. Mahraz, *Chalco. Lett.*, **11**, 111 (2014).
4. S. Arunkumar, K. V. Krishnaiah, and K. Marimuthu, *Physica B*, **416**, 88 (2013).
5. N. Elkhoshkhany, E. Syala, and E. S. Yousef, *Results Phys.*, **14**, 102370 (2019).
6. K. Tanaka, Y. Toshinobu, H. Yamada, and K. Kamiya, *J. Alloys Compd.*, **103**, 250 (1988).
7. Y. Iwadate, H. Kenmotsu, and T. Hattori, *J. Alloys Compd.*, **305**, 130 (2000).
8. M. M. Umair and A. K. Yahya, *Chalcogenide Letters.*, **12**, 287 (2015).
9. S. Azianty, A. K. Yahya, and M. K. Halimah, *Mater. Chem. Phys.*, **142**, 549 (2012).
10. M. R. Tripathy, R. Joshi, N. C. Mehra, S. Kumar, and R. P. Tandon, *Mater. Lett.*, **61**, 585 (2007).
11. S. Chakraborty, H. Satou, and H. Sakata, *J. Appl. Phys.*, **82**, 5520 (1997).
12. A. A. Ali and M. H. Shaaban, *Solid State Sci.*, **12**, 2148 (2010).
13. M. Abdel-Baki, A. M. Salem, F. A. Abdel-Wahab, and F. El-Diasty, *J. Non-Cryst. Solids*, **354**, 4527 (2008).
14. D. D. Ramteke and R. S. Gedam, *Solid State Ionics*, **258**, 82 (2014).
15. A. L. Moura, L. J. Q. Maia, V. Jerez, A. S. L. Gomes, and C. B. de Araújo, *J. Lumin*, **214**, 116543 (2019).
16. M. Kaky Kawa, G. Lakshminarayana, S. Baki, I. Kityk, Y. Taufiq-Yap, and M. Mahdi, *Results Phys.*, **7**, 166 (2017).
17. M. H. Shaaban, A. A. Ali, and L. K. El-Nimr, *J. Mater. Chem. Phys.*, **96**, 423 (2006).
18. M. Haouari, F. B. Slimen, A. Maaoui, and N. Gaumer, *J. Alloy. Compd.*, **743**, 586 (2018).
19. M. Ribes, J. R. Akridge, and M. Balkanski, *Solid State Microbatteries* (Springer, New York) (1990).
20. V. B. Sreedhar, K. V. Krishnaiah, S. K. N. Rasool, V. Venkatramu, and C. K. Jayasankar, *J. Non-Cryst. Solids*, **505**, 115 (2019).
21. S. K. Gupta, H. Abdou, C. U. Segre, Y. Mao, and Y. Nanomaterials, **12**, 3028 (2022).
22. A. Volokitina, P. Loiko, E. Dunina, A. Kornienko, J. M. Serres, M. Aguiló, F. Díaz, A. Pavlyuk, X. Mateo, and J. Phys, *Conf. Ser*, **2086**, 012175 (2021).
23. R. S. Gedam and D. D. Ramteke, *J. Phys. Chem. Solids*, **74**, 1399 (2013).
24. H. A. A. Sidek, S. Rosmawati, Z. A. Talib, M. K. Halimah, and W. M. Daud, *Am. J. App. Sci.*, **6**, 1489 (2009).
25. G. Upender, S. Ramesh, M. Prasad, V. G. Sathe, and V. C. Mouli, *J. Alloy. Compd.*, **504**, 468 (2010).
26. S. Rada, A. Dehelean, and E. Culea, *J. Non-Cryst. Solids*, **357**, 3070 (2011).
27. R. S. Gedam, D. D. Ramteke, and J. Rare, *Earth.*, **30**, 785 (2012).
28. I. Jlassi, N. Sdiri, H. Elhouichet, and M. Ferid, *J. Alloy. Compd.*, **645**, 125 (2015).
29. M. P. Kumar, T. Sankarappa, and S. Kumar, *J. Alloy. Compd.*, **464**, 393 (2008).
30. P. R. Rao, L. Pavić, A. Moguš-Milanković, V. R. Kumar, I. V. Kityk, and N. Veeraiah, *J. Non-Cryst. Solids*, **358**, 3255 (2012).
31. G. Gruener, D. D. S. Meneses, P. Odier, and J. P. Loup, *J. Non-Cryst. Solids*, **281**, 117 (2001).
32. R. S. Gedam and D. D. Ramteke, *J. Phys. Chem. Solids*, **74**, 1039 (2013).
33. A. K. Jonscher, *universal Relaxation Law* (Chelsea Dielectrics Press, London) (1996).
34. S. Hraiech and M. Ferid, *J. Alloy. Compd.*, **577**, 543 (2013).
35. Y. B. Saddeek, *J. Alloy. Compd.*, **467**, 14 (2009).
36. Y. Gandhi, I. V. Kityk, M. G. Brik, P. R. Rao, and N. Veeraiah, *J. Alloy. Compd.*, **508**, 278 (2010).
37. P. S. Rao, C. Rajyasree, A. R. Babu, P. M. V. Teja, and D. K. Rao, *J. Non-Cryst. Solids*, **357**, 3585 (2011).
38. P. S. Rao, P. R. Babu, R. Vijay, T. Narendrudu, N. Veeraiah, and D. K. Rao, *Mater. Res. Bull.*, **57**, 58 (2014).
39. K. Srilatha, K. S. Rao, Y. Gandhi, V. Ravikumar, N. Veeraiah, and J. Alloy, *Compd.*, **507**, 391 (2010).
40. M. S. Reddy, N. G. Raju, G. Nagarjuna, and N. Veeraiah, *J. Alloy. Compd.*, **438**, 41 (2007).
41. M. Nagarjuna, P. Raghava Rao, Y. Gandhi, V. Ravikumar, and N. Veeraiah, *Physica B*, **405**, 668 (2010).
42. D. D. Ramteke and R. S. Gedam, *Spectrochimica acta. Part A.*, **133**, 19 (2014).
43. R. M. Mahani and S. Y. Marzouk, *J. Alloy. Compd.*, **579**, 394 (2013).
44. N. A. Hegab and H. M. El-mallah, *Acta Phys. Pol. A*, **116**, 1048 (2009).
45. S. M. Salem, E. K. Abdel-Khalek, E. A. Mohamed, and M. A. Farouk, *J. Alloy. Compd.*, **513**, 35 (2012).
46. S. Z. A. Ahamed, C. M. Reddy, and B. D. P. Raju, *J. Spectrochim. Acta A.*, **103**, 246 (2013).
47. E. A. Davis and N. F. Mott, *Philos. Mag.*, **22**, 903 (1970).
48. R. P. Sreekanth Chakradhar, K. P. Ramesh, J. L. Raob, and J. Ramakrishna, *J. Phys. Chem. Solids*, **64**, 641 (2003).
49. E. Wu, H. Chen, Z. Sun, and H. Zeng, *J. Opt. Lett.*, **28**, 1692 (2003).
50. F. Urbach, *Phys. Rev.*, **92**, 1324 (1953).
51. B. D. Mcswain, N. F. Borrel, and S. V. Gongjen, *J. Phys. Chem. Glasses.*, **1**, 4 (1963).
52. S. Akamine, T. Nanba, Y. Miura, and S. Sakida, *9th biennial worldwide congress on refractories.*, 8 (2005).
53. A. Berthereau, E. Fargin, A. Villezusanne, R. Olazcuaga, G. Le Flem, L. Ducasse, and J. Solid, *State. Chem.*, **126**, 142 (1996).
54. B. D. P. Raju and C. M. Reddy, *Optic. Mater.*, **34**, 1251 (2012).
55. C. R. Kesavulu, K. K. Kumar, N. Vijaya, and K. S. Lim, *Mater. Chem. Phys.*, **141**, 903 (2013).
56. T. Som and B. Karmakar, *J. Phys. Condens. Matter*, **22**, 035603 (2010).
57. T. S. Barros, B. S. Barros, S. Alves, R. H. G. Kiminami, H. L. Lira, and A. C. F. M. Costa, *Mater. Sci. Forum.*, **591**, 745 (2008).
58. W. Stambouli, H. Elhouichet, B. Gelloz, and M. Férid, *J. Lumin.*, **138**, 201 (2013).
59. K. Maheshvaran and K. Marimuthu, *J. Lumin.*, **132**, 2259 (2012).
60. P. Krishnapuram, S. K. Jakka, C. Thummala, and R. M. Lalapeta, *J. Mol. Struct.*, **1028**, 170 (2012).